

36 Plain Language Summary

37 Large earthquakes modify the state of stress and pore pressure in the upper crust and mantle.
38 These changes induce stress relaxation processes and pore pressure diffusion in the postseismic
39 phase. The two main stress relaxation processes are postseismic slip along the rupture plane of
40 the earthquake and viscoelastic deformation in the rock volume. These processes decay with
41 time, but can sustain over several years or decades, respectively. The other process that results in
42 volumetric crustal deformation is poroelasticity due to pore pressure diffusion, which has not
43 been investigated in detail. Using postseismic surface displacement data acquired by radar
44 satellites after the 2010 Maule earthquake, we show that poroelastic deformation may
45 considerably affect the vertical component of the observed geodetic signal during the first
46 months. Poroelastic deformation also has an impact on the estimation of the postseismic slip,
47 which in turn affects the energy stored at the fault plane that is available for the next event. In
48 addition, shallow aftershocks within the continental crust show a good, positive spatial
49 correlation with regions of increased postseismic pore-pressure changes, suggesting they are
50 linked. These findings are thus important to assess the potential seismic hazard of the segment.

51

52 1. Introduction

53 In the aftermath of large earthquakes, the Earth surface displays time-dependent deformation
54 patterns on different spatiotemporal scales that may last several of years or decades due to the
55 relaxation of coseismically imposed stress and pore pressure changes in the lithosphere-
56 asthenosphere system (e.g., Hergert and Heidbach, 2006; Hughes et al., 2010; Wang et al., 2012,
57 and references therein). These relaxation processes are aseismic postseismic slip on the fault
58 interface (afterslip), poroelastic processes in the upper crust, and viscoelastic relaxation in the
59 lower crust and upper mantle (e.g., Barbot, 2018; Hughes et al., 2010; Peña et al., 2020; Sun and
60 Wang, 2015). Afterslip distributions can be used as a proxy to gain valuable insights into the
61 mechanical behavior of the fault interface and to quantify the remaining slip budget (Avouac,
62 2015, and references therein). To do so, it is compulsory to decipher the relative contribution of
63 each postseismic process to the surface deformation. In particular, the contribution of poroelastic
64 processes is not fully understood.

65 In the long-term (years to decades) and at larger spatial scales (100s of km) it is widely accepted
66 that afterslip and viscoelastic relaxation prevail (e.g. Peña et al., 2020; 2021; Barbot, 2018; Sun
67 et al., 2014; Wang et al., 2012). Conversely, poroelastic processes seem to contribute primarily
68 in the early postseismic phase (days to months), especially in the near field close to the area of
69 high coseismic slip. Here, the contribution of poroelastic processes to the surface deformation
70 has been shown to be up to 30% compared to those due to linear viscoelastic relaxation (e.g., Hu
71 et al., 2014; Hughes et al., 2010; Masterlark et al, 2001). However, previous studies often neglect
72 both poroelastic and viscoelastic relaxation, assuming that afterslip is the dominant process and
73 that the crust and upper mantle respond in a purely elastic fashion (e.g., Aguirre et al., 2019;
74 Rolandone et al., 2018; Tsang et al., 2019). Recently McCormack et al. (2020) and Yang et al.

75 (2022) investigated the poroelastic effects on afterslip inversions during the first ~ 1.5 months
76 following the 2012 M_w 7.8 Nicoya, Costa Rica, and 2015 M_w 8.3 Illapel, Chile, earthquakes,
77 using Global Navigation Satellite System (GNSS) data. They show that the resulting amplitude
78 of afterslip may be affected by more than $\pm 50\%$ in regions of $\sim 40 \times 40 \text{ km}^2$ when neglecting
79 poroelasticity. Yet, their models ignore viscoelastic relaxation. For the same 2015 Illapel event
80 and similar postseismic 3D GNSS data, Guo et al. (2019) find that linear viscoelastic effects may
81 increase and reduce the resulting inverted afterslip at shallower and deeper segments,
82 respectively, but they do not consider the potential effect of poroelastic and non-linear
83 viscoelastic processes. Hence, the relative contributions of postseismic processes to the early
84 postseismic phase at subduction zones are still elusive.

85 The postseismic deformation associated with the 2010 M_w 8.8 Maule earthquake in central-
86 southern Chile (Figure 1) has been studied extensively using afterslip only (e.g., Aguirre et al.,
87 2019; Bedford et al., 2013), combining afterslip and linear viscoelastic relaxation (e.g., Klein et
88 al., 2016; Bedford et al., 2016), and afterslip and non-linear viscoelastic relaxation (Peña et al.,
89 2019; 2020; Weiss et al., 2019). In this work, we investigate for the first time the relative
90 contribution of afterslip, poroelastic and non-linear viscoelastic processes of the early
91 postseismic deformation of the 2010 Maule earthquake. We use a model approach that combines
92 a 4D forward model of poroelastic and non-linear viscoelastic relaxation with an afterslip
93 inversion. We use displacements observed by continuous 3D GNSS sites and Interferometric
94 Synthetic-Aperture Radar (InSAR) during the first 48 days after the main shock. We find that
95 particularly in the near field poroelastic processes significantly affect the afterslip estimates and
96 could explain the observed postseismic uplift signal.

97

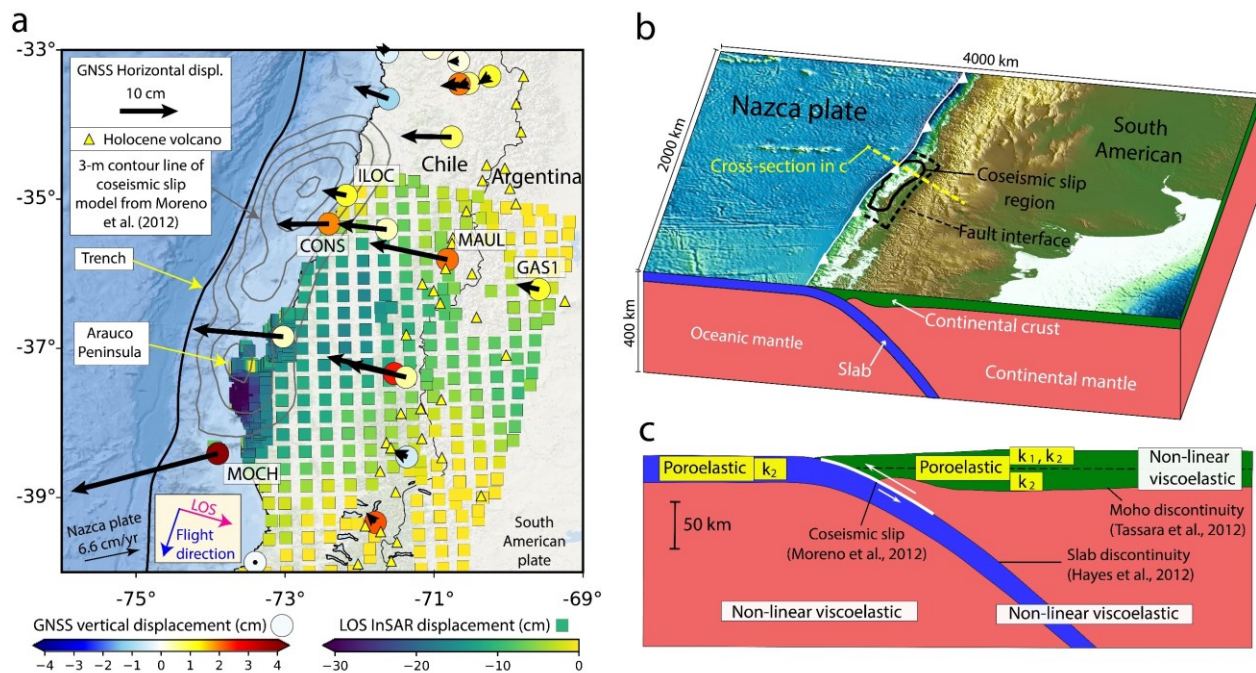
98 **2. Geodetic observations**

99 3D GNSS displacements time-series are obtained using the processing strategy explained in
100 Bedford et al. (2020). Data are retrieved in the International Terrestrial Reference Frame (ITRF)
101 2014 and then rotated to a Stable South American reference frame. Seasonal signals and offsets
102 caused by aftershocks are removed using sparse linear regression of a modified trajectory model
103 (Bedford and Bevis, 2018). We do not remove the interseismic component because it is
104 negligible compared to the surface deformation in the first 48 days. We select only stations that
105 account for at least 38 daily solutions, resulting in 20 GNSS sites (Figure 1). We linearly
106 interpolate gaps in the time series up to 10 days assuming linear behavior (e.g., Bedford et al.,
107 2013; Moreno et al., 2012).

108 To increase the spatial coverage, we complete the GNSS data with InSAR line-of-sight (LOS)
109 displacement. We used an image pair of the L-Band (23.6 cm wavelength) ALOS PALSAR
110 satellite mission from the Japanese Space Agency. The scenes were acquired on descending pass
111 in ScanSAR wide-beam mode on the 1st of March (Scene ID: ALPSRS218444350) and 16th of
112 April (ALPSRS225154350), thus spanning day 2 to 48 following the earthquake. The differential
113 interferogram was created after co-registration and burst synchronization using the GAMMA

114 software (Wegmüller and Werner, 1997; Werner et al., 2011). To increase the coherence, we
 115 multi-looked the original interferogram 3, resp., 16 times in range/azimuth to a spatial resolution
 116 of 30/50 m. We removed the topographic phase using a 90 m digital elevation model from the
 117 Shuttle Radar Topography Mission (Farr et al., 2007). We further improved the signal-to-noise
 118 ratio with an adaptive phase filter (Goldstein & Werner, 1998) and unwrapped the phase using
 119 Minimum Cost Flow (Costantini, 1998). The geocoded LOS displacements were quad-tree
 120 subsampled (Welstead, 1999; Jónsson et al., 2002) to a total number of 586 data samples using
 121 the Kite software (Isken et al., 2017) from the open-source seismology toolbox Pyrocko
 122 (Heimann et al., 2017). Uncertainties were estimated using the full variance-covariance matrix
 123 (Sudhaus and Jónsson, 2009). Finally, we removed the long-wavelength orbital signal by
 124 minimizing the misfit between the LOS InSAR displacements (averaged on a $15 \times 15 \text{ km}^2$
 125 window at each GNSS position) and the GNSS data (collapsed into LOS) using a linear ramp
 126 (e.g., Cavalié et al., 2013). The GNSS and deramped InSAR data are then used for the afterslip
 127 inversion.

128



129

130 Figure 1. a) Cumulative postseismic InSAR and GNSS surface displacements between the days 2
 131 and 48 after the 2010 Maule M_w 8.8 earthquake. Negative LOS values indicate relative motion
 132 away from the satellite. b) 3D view and c) cross-section of the model illustrating layers and
 133 rheology with k as permeability described in section 3.

134

135

136

137 **3. Model setup**

138 We use the model workflow of Peña et al. (2020), where the postseismic surface displacements
 139 produced by 4D forward simulation are first subtracted from the geodetic data. The remaining
 140 signal is then inverted for afterslip. Here, we extend the forward model part of Peña et al. (2020)
 141 by adding poroelasticity to the model (Figure 1c).

142 We simulate the postseismic non-linear rock viscous deformation under high-temperature and
 143 high-pressure conditions as:

$$\dot{\epsilon}_{cr} = A\sigma^n \exp\left(\frac{-Q}{RT}\right) \quad (1)$$

144 where $\dot{\epsilon}_{cr}$ is the creep strain rate, A is a pre-exponent parameter, σ the differential stress, n the
 145 stress exponent, Q the activation energy for creep, R the gas constant and T the absolute
 146 temperature (e.g., Hirth & Kohlstedt, 2003). The poroelastic response is simulated following the
 147 approach of Wang (2000), where the constitute equations of mass conservation and Darcy's law
 148 describe the coupled displacement (u) and pore-fluid pressure (p) in Cartesian coordinates (x)
 149 expressed in index notation as follows:

$$G\nabla^2 u_i + \frac{G}{(1-2\nu)} \frac{\partial^2 u_k}{\partial x_i \partial x_k} = \alpha \frac{\partial p}{\partial x_i} \quad (2)$$

150

$$\alpha \frac{\partial \epsilon_{kk}}{\partial t} + S_\epsilon \frac{\partial p}{\partial t} = \frac{k}{\mu_f} \nabla^2 p \quad (3)$$

151 Here, G and ν are the shear modulus and the drained Poisson ratio, respectively, α is the Biot-
 152 Willis coefficient, t the elapsed time since the main shock, S_ϵ the constrained storage coefficient,
 153 $\epsilon_{kk} = \partial u_k / \partial x_k$ is the volumetric strain, k the intrinsic permeability and μ_f the pore-fluid viscosity
 154 (Wang, 2000). The subscript i represents the three orthogonal spatial directions, while the
 155 subscript k denotes the summation over these three components (Hughes et al., 2010).

156 The onset of the poroelastic and viscoelastic postseismic deformation is driven by the
 157 coseismically induced response (e.g., Hughes et al., 2010; Masterlark et al., 2001; MacCormarck
 158 et al., 2020). We prescribe the coseismic slip model of Moreno et al. (2012) as displacement
 159 boundary conditions on the fault interface (Peña et al., 2020). The lateral and bottom model
 160 boundaries are free to displace parallel to their faces. We also apply stress-free and no-flow
 161 boundary conditions in the surface layer (e.g., Hughes et al., 2010; Tung and Masterlark, 2018).
 162 The resulting numerical problem is solved with the commercial finite element software
 163 ABAQUSTM, version 6.14.

164 Given the high uncertainty of rock permeability, temperature, and viscous creep parameters, we
 165 consider end-member scenarios for the crust and upper mantle (Figure 1c; Tables S1 and S2).
 166 We consider two scenarios with lower and upper bounds of permeability of $1 \times 10^{-16} \text{ m}^2$ and
 167 $1 \times 10^{-14} \text{ m}^2$ for the continental crust in the upper 15 km (Völker et al., 2011), while we set a

168 permeability of $1 \times 10^{-16} \text{ m}^2$ for the lower crust, as obtained from crustal-scale studies in Chile
169 (e.g., Husen and Kissling, 2001; Koerner et al., 2004) and other regions (e.g., Ingebritsen and
170 Manning, 2010). We adopt quartzite and diabase creep parameters for the continental crust, and
171 wet olivine with 0.01 and 0.005 percent of water for the upper mantle (e.g., Hirth & Kohlstedt,
172 2003; Peña et al., 2020). We do not further explore rock property changes for the oceanic crust
173 and mantle due to the lack of offshore measurements to constrain our results. We thus set a
174 permeability of $1 \times 10^{-16} \text{ m}^2$ for the oceanic plate (Fisher, 1998), and assign diabase and wet
175 olivine with 0.005 percent of water creep parameters for the slab and oceanic mantle,
176 respectively (Peña et al., 2020).

177 During the afterslip inversion, we determine the relative weights of InSAR and GNSS data sets
178 by identifying the optimal misfit value between the observed and modelled surface displacement
179 that does not substantially vary the misfit of each individual data set (e.g., Cavalié et al., 2013;
180 Melgar et al., 2017). We find that the relative weights for GNSS and InSAR are 1 and 0.6,
181 respectively (Figure S2). This agrees with the tendency of lowering the InSAR data weight when
182 including GNSS and InSAR along with land-leveling (Moreno et al., 2012) and strong motion
183 data (Melgar et al., 2017) that found relative weights of about 0.5 and 0.3 for GNSS and InSAR
184 data, respectively. Furthermore, we neglect the postseismic processes coupling as it does not
185 change the results beyond the GNSS data uncertainty (Figure S3).

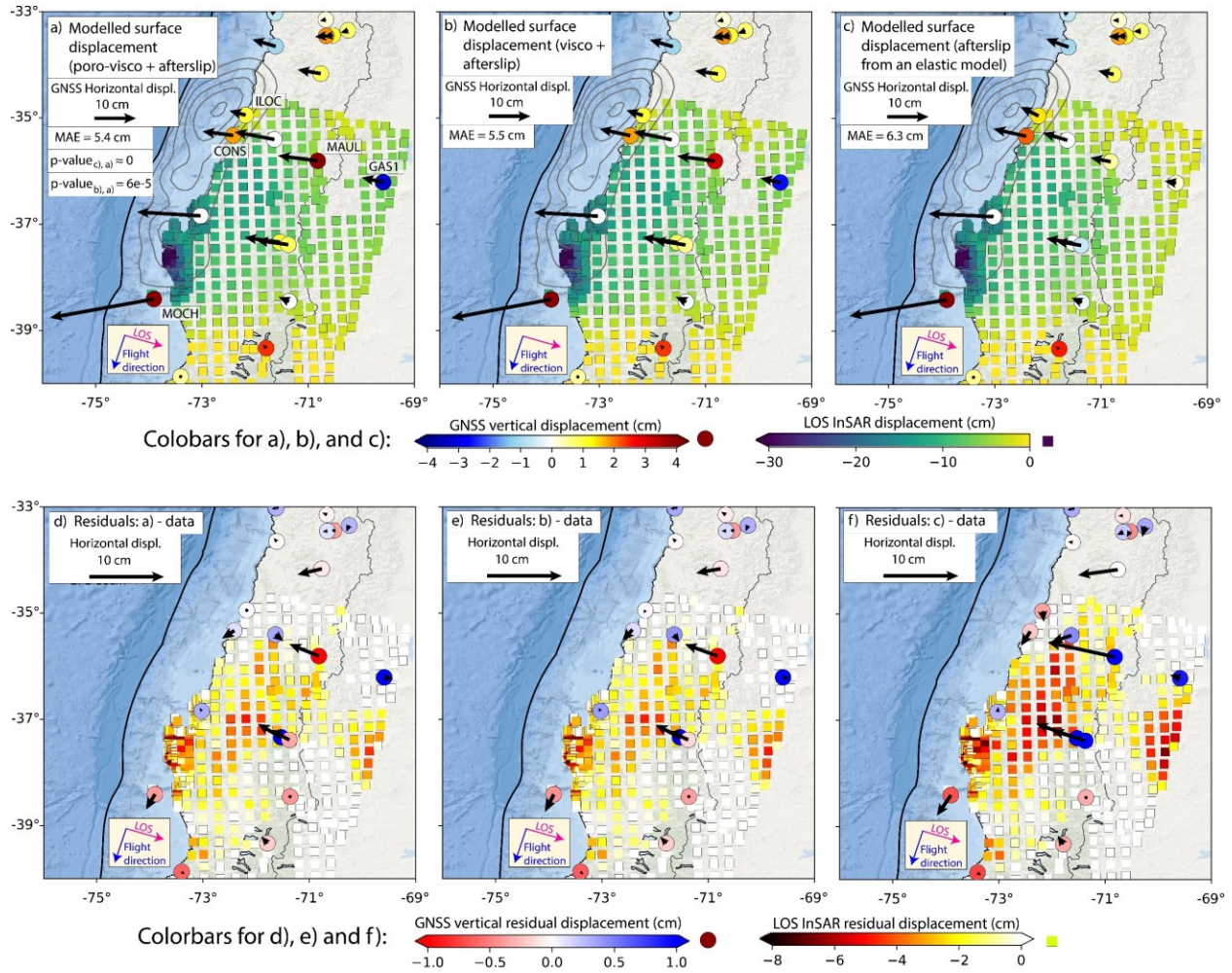
186

187 **4. Model results compared to geodetic observations**

188 All GNSS horizontal postseismic displacements show trench-ward motion (Figure 1). The
189 maximum cumulative surface displacement reaches 24.5 cm at station MOCH, while the
190 maximum cumulative InSAR LOS displacement is observed at the Arauco Peninsula with
191 32.5 cm. The volcanic arc region also exhibits significant long-wavelength deformation, reaching
192 ~ 15 cm and ~ 2 cm in the horizontal and vertical components at the station MAUL, respectively.
193 Along the coastline, the observations exhibit strong vertical variations. The northern part
194 subsides by up to 1 cm, while the two GNSS sites (ILOC and CONS) near the region of
195 maximum coseismic slip yield uplift of 1-2 cm. A maximum uplift of 6.5 cm is measured at
196 station MOCH further south.

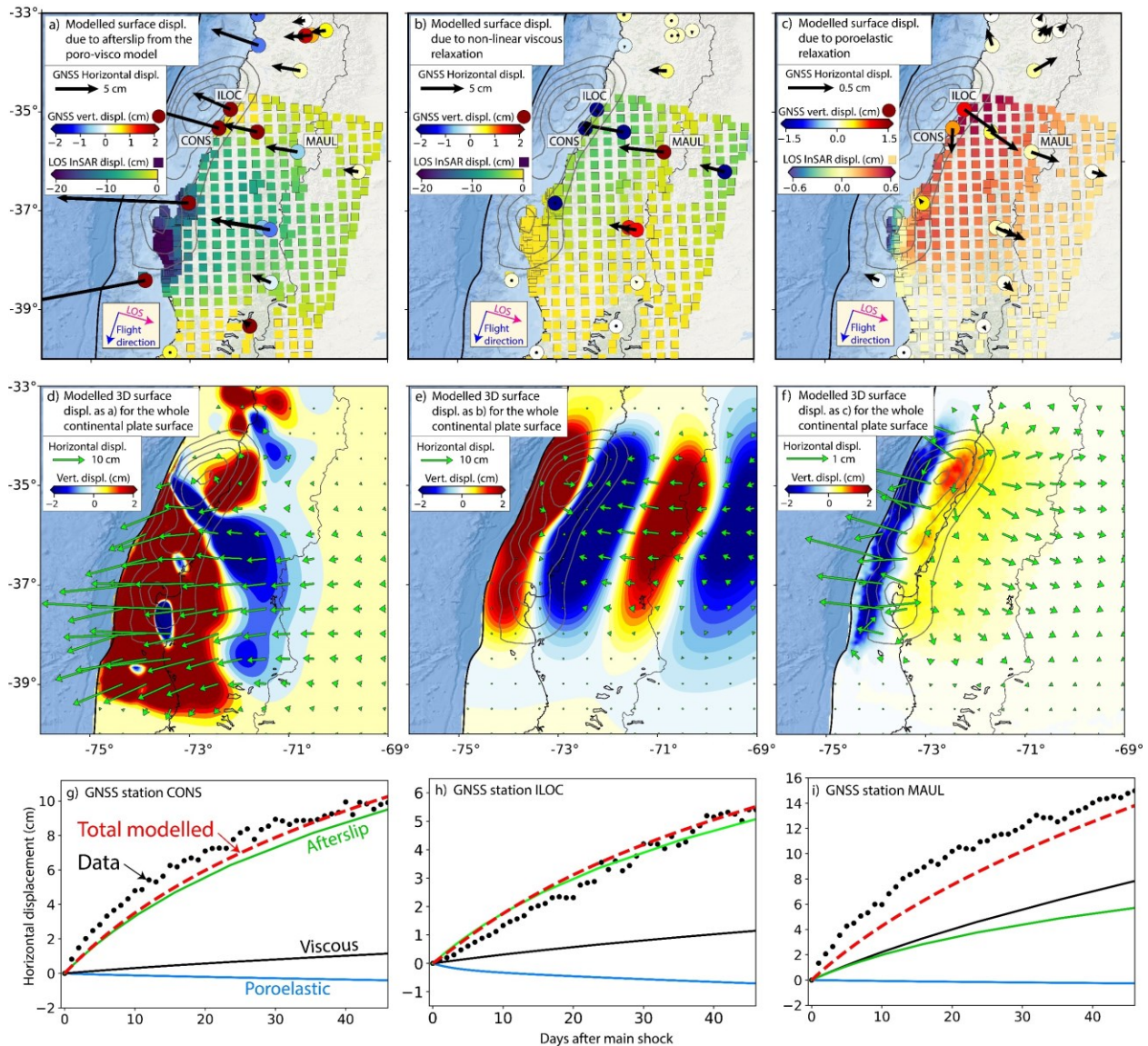
197 The combined result of the forward poro-viscoelastic model and the afterslip inversion display a
198 lowest mean absolute data error of 5.4 cm (Figure 2a; Table S3), while by neglecting
199 poroelasticity the data misfit slightly increases to 5.5 cm (Figure 2b). Despite this small data fit
200 improvement, our F-test results show that our poro-viscoelastic model is statistically better than a
201 (non-linear) viscoelastic-only model considering a significance level of 0.05 (Figure 2a and
202 Supp. Information). The data fit of the poro-viscoelastic model is 14% better than the one from a
203 pure elastic model (Figure 2c and 2f). In particular, the inclusion of viscoelasticity can
204 substantially improve the data fit in the volcanic and back-arc regions and, to some extent, at the
205 coast (Figure 2d and 2e).

206 We also show that afterslip processes dominate the near-field deformation (Figure 3a, 3d, and
 207 3g), while non-linear viscoelastic relaxation the surface deformation at volcanic and back arc
 208 regions (Figure 3b, 3e, and 3i). The largest poroelastic effects are found close to the region of
 209 maximum coseismic slip, while the resulting surface poroelastic response exhibit varying
 210 patterns (Figure 3f). Onshore, the poroelastic response exhibits landward and uplift surface
 211 deformation, while offshore and particularly close to the trench it is the opposite (Figure 3f). The
 212 cumulative poroelastic landward displacements reach up to 0.75 cm, lowering the cumulative
 213 displacement of station ILOC by ~15% (Figure 3c and 3h). We also find that the poroelastic
 214 response exhibits a maximum coastal uplift of 1.3 cm (Figure 3c and 3f), which is in good
 215 agreement with the observations.



216

217 Figure 2. Predicted displacements from forward modelling in combination with an afterslip
 218 inversion considering a) poroelasticity and non-linear viscoelasticity, b) non-linear
 219 viscoelasticity-only, and c) elasticity-only. MAE represents the mean absolute error. The p-
 220 values in a) are obtained by computing the F-values from b) and c) (null hypothesis) with respect
 221 to a). d), e) and f) show the residual displacements between the model in a) and c) and the
 222 geodetic data.



224

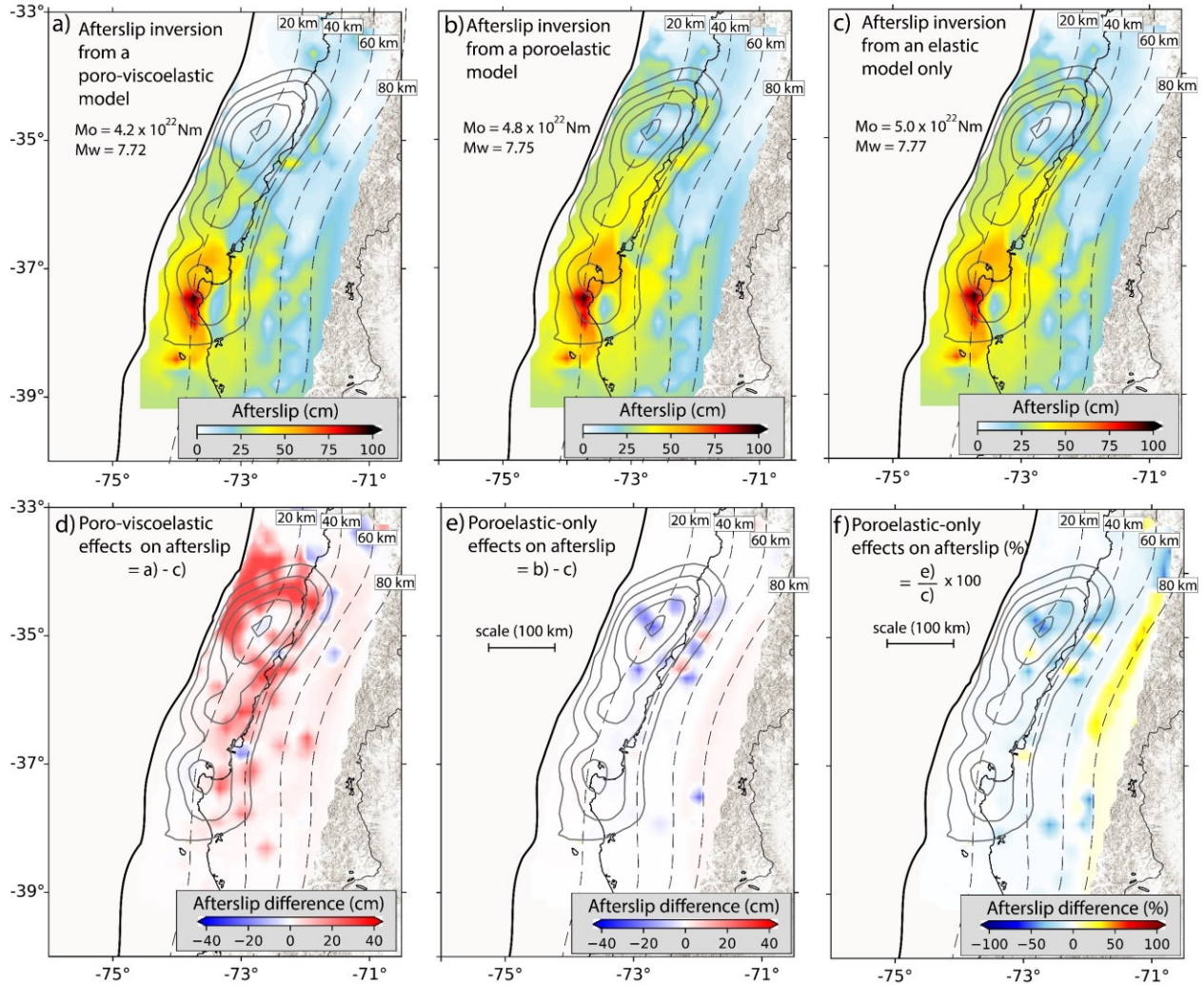
225 Figure 3. Decomposition of the predicted cumulative and temporal 3D surface displacements
 226 from the model that inverts for afterslip considering poro-viscoelasticity. Individual contribution
 227 due to a) afterslip, b) viscoelastic, and c) poroelastic processes at the observation sites and d), e),
 228 and f) in full 3D-resolution. Individual GNSS horizontal time-series decomposition at stations
 229 CONS g), ILOC h) and MAUL i). Temporal evolution of afterslip is modelled with a logarithmic
 230 function as $A(t) = A_0 \log((t + t_c)/t_r)$, where A_0 is the cumulative afterslip calculated from the
 231 inversion approach, t is the time after the main shock, t_r is the characteristic time of relaxation,
 232 and t_c the critical time, which is introduced to avoid the singularity at $t = 0$ (Avoauc et al., 2015).

233

234

235 **5. Spatial distributions of afterslip**

236 We further compare afterslip distributions resulting from a poro-viscoelastic, poroelastic and
237 elastic models. Overall, these models predict most of the afterslip occurring outside regions of
238 high coseismic slip (Figure 4a and 4c), with maximum afterslip amplitude in the southern
239 segment at 37.7°S at 20 km depth. In the northern segment, however, the afterslip predicted by
240 the poro-viscoelastic model differs. It is notably reduced by more than 30 cm close to the trench
241 and by 20-30 cm at 20-50 km depths (Figure 4d). At 20-50 km depth, afterslip resolution and
242 bootstrapping tests report robust results (Figure S4 and S5; Bedford et al., 2013; Peña et al.,
243 2020). We find a general reduction of the afterslip by 16% if poro-viscoelastic effects are
244 incorporated. Viscoelastic effects dominate the prediction as the poroelastic effects (Figure 4e)
245 are significantly smaller than those from the combined model (Figure 4d). However, poroelastic
246 effects alter the afterslip distribution by up to ± 25 cm in regions of $\sim 50 \times 50$ km² (Figure 4e),
247 representing up to $\pm 40\%$ of deviation from the elastic-only model (Figure 4f). These effects are
248 strongest near the region of maximum coseismic slip, where poroelastic effects contribute most
249 to the observed surface displacements (Figure 3c).



250

251 Figure 4. Afterslip distributions from a) the poro-viscoelastic, b) the poroelastic-only and c) the
 252 elastic-only models. Grey contour lines show coseismic slip as in Figure 1. Dashed lines
 253 represent the plate interface depth from Hayes et al. (2012). d) and e) exhibit afterslip
 254 differences between a) and b), and b) and c), respectively, while f) as e) but in percent.

255

256

257

258

259

260

261

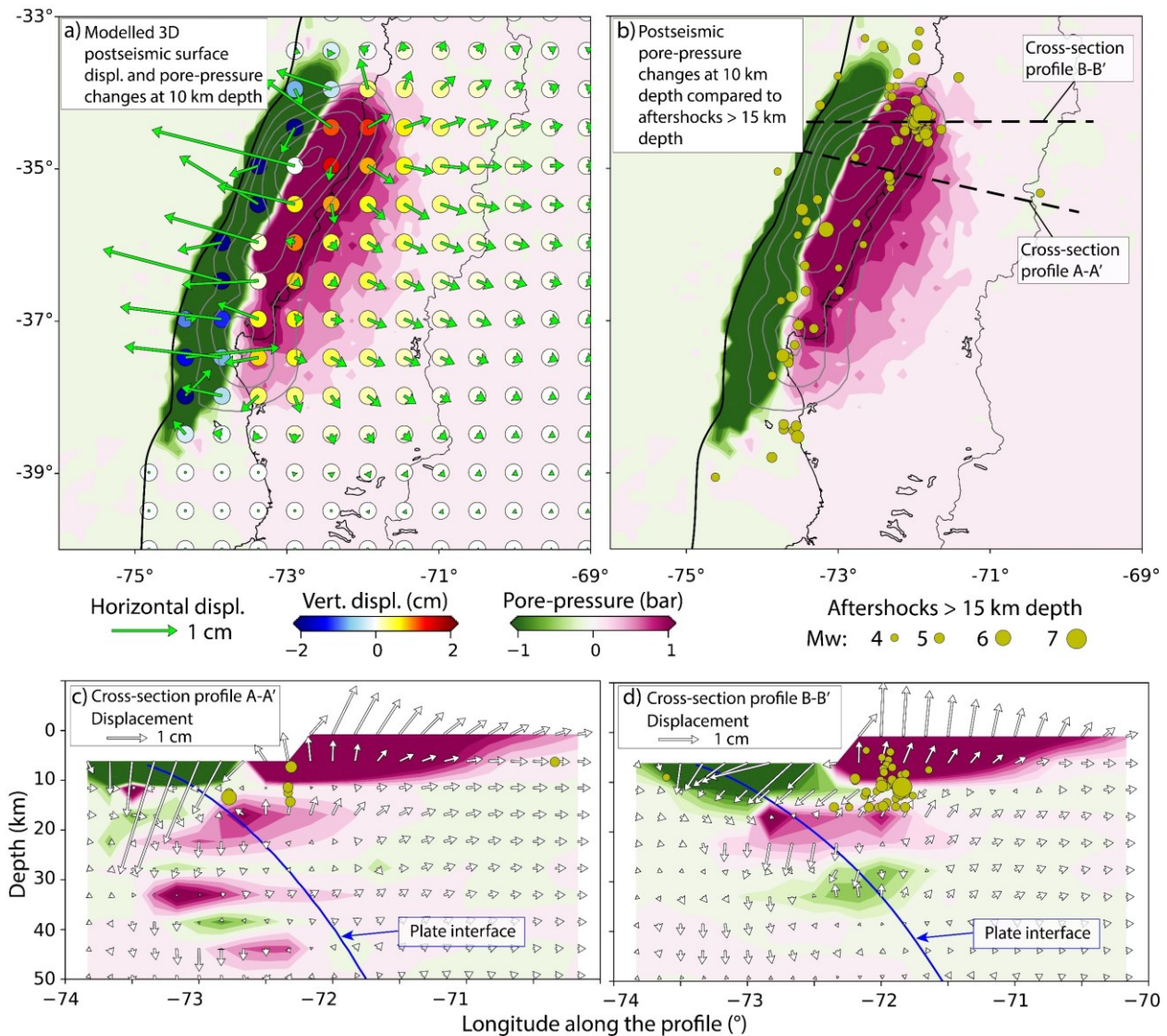
262

263 6. Discussion

264 Poroelastic processes in the upper crust are a fundamental aspect of rock mechanics (e.g., Beeler
265 et al., 2000; Oncken et al., 2021; Warren-Smith et al., 2018). Yet, they have been commonly
266 ignored in postseismic deformation studies. We show that following the Maule event, poroelastic
267 processes affect horizontal GNSS observations by up to 15% (Figure 3c). Moreover, poroelastic
268 processes locally alter the estimated afterslip by up to $\pm 40\%$ near the region of maximum
269 coseismic slip compared to the results of a purely elastic model. Similar patterns have been also
270 reported for the 2012 Nicoya Costa Rica (McCormack et al., 2020) and the 2015 Illapel Chile
271 (Yan et al., 2022) earthquakes. Nonetheless, in the work by McCormack et al. (2020) and Yang
272 et al. (2022) the poroelastic effects on both the geodetic signal and afterslip amplitudes are
273 generally larger than in our study. This might be because these studies neglect viscoelastic
274 relaxation, which also has a significant impact on the afterslip distributions (Figure 4d). In
275 particular, the inclusion of non-linear viscoelasticity considerably reduces the afterslip at
276 shallower segments close to the region of largest coseismic slip (Figure 4a and 4d), thus better
277 explaining the absence of shallow aftershocks (e.g., Lange et al., 2012) (Figure S6).

278 Our poro-viscoelastic model considers rock parameters that agree with previous studies
279 investigating non-linear viscoelastic (Peña et al., 2020; 2021; Weiss et al., 2019) and poroelastic
280 processes (e.g., Koermer et al., 2004). The permeability of 10^{-14} m^2 used here, however, is about
281 two orders of magnitude higher than that the one used by studies investigating the postseismic
282 deformation of the 2011 Tohoku-Oki (Hu et al., 2014) and the 2004 Sumatra-Andaman
283 megathrust events (Hughes et al., 2010). Nevertheless, these authors either focused on a longer
284 observation period (~ 2 yrs, Hu et al., 2016) or investigated the stress transfer due to pore-
285 pressure changes (Hughes et al., 2010). This relatively high permeability may be because of
286 upper crustal fractures augmenting permeability locally (e.g., Golima et al., 2016) or a transient
287 response increasing permeability due to the pass of the seismic waves (e.g., Manga et al., 2012),
288 or both processes.

289



290

291 Figure 5. Cumulative postseismic pore-pressure changes, displacement, and $M_w \geq 4$ aftershock
 292 distribution in the upper 15 km (USGS-NEIC catalogue) during the first 48 days following the
 293 main shock.

294

295 Our results show that the predicted poroelastic vertical displacement is about two times higher
 296 than the horizontal displacement (Figure 3f), which is in good agreement with previous studies
 297 (Hu et al., 2014; Hughes et al., 2010; Masterlark et al., 2001; McCormack, et al., 2020).
 298 Poroelastic vertical surface displacement patterns can also explain a major part of the observed
 299 uplift near the maximum coseismic slip region (Figure 3c). The modelled surface uplift and
 300 subsidence pattern is produced by increase and decrease of postseismic pore-pressure changes in
 301 the upper crust following the main shock, respectively (Figure 5a and 5c). We also find that
 302 shallow aftershocks, especially above ~ 11 km depth, mostly occur beneath the coastal forearc,
 303 where our model predicts pore-pressure increase (Figure 5b-d). An increase of shallow seismic

304 activity following megathrust earthquakes has been observed in many subduction zones (e.g.,
305 Soto et al., 2019; Toda et al., 2011), but the mechanisms of these aftershocks are not well
306 understood. Our results indicate that increased postseismic pore-pressure changes may be a
307 plausible triggering process, as they reduce the effective fault normal stress more efficiently than
308 afterslip and viscous processes (e.g., Hughes et al., 2010; Miller et al., 2004).

309 Given that the vertical surface displacement is highly sensitive to poroelastic effects (Figure 3f),
310 additional geodetic vertical deformation data derived from, for example, offshore pressure
311 gauges (Wallace et al., 2016) or multiple radar look directions (Wright et al., 2004) could be
312 used in future studies to better understand crustal poroelastic processes. Moreover, a
313 homogenous spatial distribution of permeability may not be a realistic representation of the
314 upper crust (e.g., Manga et al., 2012). Additional water-level observations could directly
315 constrain spatial variations of crustal poroelastic properties (McCormack and Hesse, 2018).

316

317 **7. Conclusion**

318 We use a 4D forward model that considers poroelasticity and non-linear viscoelasticity to invert
319 for the afterslip during the first 48 days of postseismic deformation following the 2010 Maule
320 earthquake. Compared to a purely elastic model inverting for afterslip only, our model approach
321 fits the observed postseismic geodetic data 14% better and yields a reduction of the total
322 predicted afterslip of 16%. The latter is primarily due to the implementation of viscoelasticity.
323 Close to the area of maximum coseismic slip, poroelastic effects play a local, but significant role
324 by dragging the horizontal GNSS observations by up to 15% in the opposite direction and
325 altering the afterslip amplitude by up to $\pm 40\%$ in regions of $\sim 50 \times 50 \text{ km}^2$. Poroelastic effects on
326 postseismic slip budgets may be higher and may play a key role in triggering upper crustal
327 aftershocks. However, additional vertical geodetic and water-level are needed to validate these
328 hypotheses and to improve our knowledge of poroelastic processes in the upper crust.

329

330

331

332

333

334

335

336

337

338

339 **Acknowledgments**

340 This work has received funding from the Initiative and Networking Fund of the Helmholtz
341 Association through the project “Advanced Earth System Modelling Capacity (ESM)”.

342

343 **Open Research**

344 GNSS data are available through Bedford et al. (2020). We use the model geometry that is
345 available in Peña et al. (2020). We use Kite software (Isken et al., 2017) from the open-source
346 seismology toolbox Pyrocko (Heimann et al., 2017). The ALOS-2/PALSAR-2 data were
347 provided by the Japanese Aerospace Exploration Agency (JAXA) under the 4th Research
348 Announcement (RA) Program and are available from <https://auig2.jaxa.jp/ips/home>.

349

350 **References**

351 Agata, R., Barbot, S.D., Fujita, K., Hyodo, M., Iinuma, T., Nakata, R., Ichimura, T., Hori, T., 2019. Rapid mantle
352 flow with power-law creep explains deformation after the 2011 Tohoku mega-quake. *Nat. Commun.*10 (1),
353 1385. <https://doi.org/10.1038/s41467-019-08984-7>.

354 Araya Vargas, J., Meqbel, N. M., Ritter, O., Brasse, H., Weckmann, U., Yáñez, G., & Godoy, B. (2019). Fluid
355 distribution in the Central Andes subduction zone imaged with magnetotellurics. *Journal of Geophysical*
356 *Research: Solid Earth*, 124, 4017– 4034. <https://doi.org/10.1029/2018JB016933>

357 Avouac, J.-P., 2015. From geodetic imaging of seismic and aseismic fault slip to dy-namic modeling of the seismic
358 cycle. *Annu. Rev. Earth Planet. Sci.*43, 233–271. <https://doi.org/10.1146/annurev-earth-060614-105302>.

359 Barbot, S. Frictional and structural controls of seismic super-cycles at the Japan trench. *Earth Planets Space* 72, 63
360 (2020). <https://doi.org/10.1186/s40623-020-01185-3>

361 Barbot, S., 2018. Asthenosphere flow modulated by megathrust earthquake cycles. *Geophys. Res. Lett.*45, 6018–
362 6031. <https://doi.org/10.1029/2018GL078197>

363 Beeler, N. M., Simpson, R. W., Hickman, S. H., and Lockner, D. A. (2000), Pore fluid pressure, apparent friction,
364 and Coulomb failure, *J. Geophys. Res.*, 105(B11), 25533–25542. <https://doi.org/10.1029/2000JB900119>

365 Bedford, J. et al. Trajectory models for daily displacement time series in the five years preceding the 2010 Maule
366 Mw 8.8, Chile, and 2011 Tohoku-oki Mw 9.0, Japan earthquakes (GFZ Data Services, 2020);
367 <https://doi.org/10.5880/GFZ.4.1.2020.001>.

- 368 Bedford, J., & Bevis, M. (2018). Greedy automatic signal decomposition and its application to daily GPS time
369 series. *Journal of Geophysical Research: Solid Earth*, 123, 6992–7003.
370 <https://doi.org/10.1029/2017JB014765>
- 371 Bedford, J., Moreno, M., Li, S., Oncken, O., Baez, J. C., Bevis, M., Heidbach, O., & Lange, D. (2016). Separating
372 rapid relocking, afterslip, and viscoelastic relaxation: An application of the postseismic straightening
373 method to the Maule 2010 cGPS. *J. Geophys. Res. Solid Earth*, 121, 7618–7638.
374 <https://doi.org/10.1002/2016JB013093>
- 375 Bedford, J., Moreno, M., Baez, J.C., Lange, D., Tilmann, F., Rosenau, M., et al. (2013). A high-resolution, time-
376 variable after slip model for the 2010 Maule Mw = 8.8, Chile megathrust earthquake, *Earth Planet. Sci.*
377 *Let.*, 383, 26–36. <https://doi.org/10.1016/j.epsl.2013.09.020>
- 378 Cavalié, O., Pathier, E., Radiguet, M., Vergnolle, M., Cotte, N., Walpersdorf, A., et al. (2013). Slow slip event in the
379 Mexican subduction zone: Evidence of shallower slip in the Guerrero seismic gap for the 2006 event
380 revealed by the joint inversion of InSAR and GPS data. *Earth and Planetary Science Letters*, 367, 52–60.
381 <https://doi.org/10.1016/j.epsl.2013.02.020>
- 382 Costantini, M., (1998). A novel phase unwrapping method based on network programming, in *IEEE Transactions on*
383 *Geoscience and Remote Sensing*, 36(3), 813-821. <http://doi.org/10.1109/36.673674>
- 384 Gomila, R., Arancibia, G., Mitchell, T. M., Cembrano, J. M., & Faulkner, D. R. (2016). Palaeopermeability structure
385 within fault-damage zones: A snap-shot from microfracture analyses in a strike-slip system. *Journal of*
386 *Structural Geology*, 83, 103–120. <https://doi.org/10.1016/j.jsg.2015.12.002>
- 387 Christensen, N., 1996. Poisson's ratio and crustal seismology. *J. Geophys. Res.* 101 (B2), 3139–3156.
388 <https://doi.org/10.1029/95JB03446>.
- 389 Farr, T. G., Rosen, P. A., Caro, E., Crippen, R., Duren, R., Hensley, S., et al. (2007). The shuttle radar topography
390 mission. *Review of Geophysics*, 45, RG2004. <https://doi.org/10.1029/2005RG000183>
- 391 Goldstein, R.M. & Werner, C.L., 1998. Radar interferogram filtering for geophysical applications, *Geophys. Res.*
392 *Let.*, 25(21), 4035–4038. <https://doi.org/10.1029/1998GL900033>
- 393 Guo, R., Zheng, Y., Xu, J., Shahid Riaz, M., (2019). Transient Viscosity and Afterslip of the 2015 Mw 8.3 Illapel,
394 Chile, Earthquake. *Bulletin of the Seismological Society of America*, 109 (6), 2567–2581.
395 <https://doi.org/10.1785/0120190114>
- 396 Heimann, Sebastian; Kriegerowski, Marius; Isken, Marius; Cesca, Simone; Daout, Simon; Grigoli, Francesco;
397 Juretzek, Carina; Megies, Tobias; Nooshiri, Nima; Steinberg, Andreas; Sudhaus, Henriette; Vasyura-
398 Bathke, Hannes; Willey, Timothy; Dahm, Torsten (2017): Pyrocko - An open-source seismology toolbox
399 and library. GFZ Data Services. <https://doi.org/10.5880/GFZ.2.1.2017.001>

400 Hergert, T., & Heidbach, O. (2006). New insights into the mechanism of the postseismic stress relaxation
401 exemplified by the 23 June Mw = 8.4 earthquake in southern Peru, *Geophys. Res. Lett.*, 30, L02307.
402 <https://doi.org/10.1029/2005GL024858>

403 Hirth, G., & Kohlstedt, D. (2003). Rheology of the upper mantle and the mantle wedge: A view from the
404 experimentalists. *Inside the subduction Factory*, 83-105. <https://doi.org/10.1029/138GM06>

405 Hu, Y., Bürgmann, R., Freymueller, J., Banerjee, P. and Wang, K. (2014). Contributions of poroelastic rebound and
406 a weak volcanic arc to the postseismic deformation of the 2011 Tohoku earthquake. *Earth, Planets and*
407 *Space*, 66(1), 106. <https://doi.org/10.1186/1880-5981-66-106>

408 Hughes, K. L., et al. (2010). Poroelastic stress-triggering of the 2005 M8. 7 Nias earthquake by the 2004 M9. 2
409 Sumatra–Andaman earthquake. *Earth and Planetary Science Letters* 293(3-4), 289-299.
410 <https://doi.org/10.1016/j.epsl.2010.02.043>

411 Husen, S. and Kissling, E. (2001); Postseismic fluid flow after the large subduction earthquake of Antofagasta,
412 Chile. *Geology* 229 (9): 847–850. [https://doi.org/10.1130/0091-7613\(2001\)029<0847:PPFATL>2.0.CO;2](https://doi.org/10.1130/0091-7613(2001)029<0847:PPFATL>2.0.CO;2)

413 Ingebritsen, S.E. and Manning, C.E. (2010), Permeability of the continental crust: dynamic variations inferred from
414 seismicity and metamorphism. *Geofluids*, 10: 193-205. <https://doi.org/10.1111/j.1468-8123.2010.00278.x>

415 Isken, Marius; Sudhaus, Henriette; Heimann, Sebastian; Steinberg, Andreas; Daout, Simon; Vasyura-Bathke,
416 Hannes (2017): Kite - Software for Rapid Earthquake Source Optimisation from InSAR Surface
417 Displacement. V. 0.1. GFZ Data Services. <https://doi.org/10.5880/GFZ.2.1.2017.002>

418 Jónsson, S., Zebker, H.A., Segall, P. & Amelung, F., (2002). Fault slip distribution of the 1999 Mw7.2 Hector Mine
419 earthquake, California, estimated from satellite radar and GPS measurements, *Bull. seism. Soc. Am.*, 92(4),
420 1377–1389.doi: <https://doi.org/10.1785/0120000922>

421 Klein, E., Fleitout, L., Vigny, C., & Garaud, J. D. (2016). Afterslip and viscoelastic relaxation model inferred from
422 the large-scale postseismic deformation following the 2010 Mw 8.8 Maule earthquake (Chile). *Geophysical*
423 *Journal International*, 205(3), 1455–1472. <https://doi.org/10.1093/gji/ggw086>

424 Koerner, A., Kissling, E., and Miller, S. A. (2004), A model of deep crustal fluid flow following the Mw = 8.0
425 Antofagasta, Chile, earthquake, *J. Geophys. Res.*, 109, B06307. <https://doi.org/10.1029/2003JB002816>

426 Lange, D., Tilmann, F., Barrientos, S.E., Contreras-Reyes, E., Methe, P., Moreno, M., Heit, B., Agurto, H., Bernard,
427 P., Vilotte, J.-P., Beck, S. (2012). Aftershock seismicity of the 27 February 2010 Mw 8.8 Maule earthquake
428 rupture zone. *Earth Planet. Sci. Lett.* 317–318, 413–425. <https://doi.org/10.1016/j.epsl.2011.11.034>.

429 Li, S., Bedford, J., Moreno, M., Barnhart, W. D., Rosenau, M., & Oncken, O. (2018). Spatiotemporal variation of
430 mantle viscosity and the presence of cratonic mantle inferred from 8 years of postseismic deformation
431 following the 2010 Maule, Chile, earthquake. *Geochemistry, Geophysics, Geosystems*, 19, 3272– 3285.

432 <https://doi.org/10.1029/2018GC007645>

433 Li, S., Moreno, M., Bedford, J., Rosenau, M., and Oncken, O. (2015), Revisiting viscoelastic effects on interseismic
434 deformation and locking degree: A case study of the Peru-North Chile subduction zone. *J. Geophys. Res.*
435 *Solid Earth*, 120, 4522–4538. <http://doi.org/10.1002/2015JB011903>

436 Lin, Y. N., Kositsky, A. P., and Avouac, J.-P. (2010). PCAIM joint inversion of InSAR and ground-based geodetic
437 time series: Application to monitoring magmatic inflation beneath the Long Valley Caldera, *Geophys. Res.*
438 *Lett.*, 37, L23301, doi:10.1029/2010GL045769.

439 Liu, S., Shen, Z., Bürgmann, R., Jónsson, S. (2020). Thin crème brûlée rheological structure for the Eastern
440 California Shear Zone. *Geology* 49 (2): 216–221. <https://doi.org/10.1130/G47729.1>

441 Luo, H., Wang, K. (2021). Postseismic geodetic signature of cold forearc mantle in subduction zones. *Nat. Geosci.*
442 14, 104–109. <https://doi.org/10.1038/s41561-020-00679-9>

443 Manga, M., Beresnev, I., Brodsky, E. E., Elkhoury, J. E., Elsworth, D., Ingebritsen, S. E., Mays, D. C., and Wang,
444 C.-Y. (2012). Changes in permeability caused by transient stresses: Field observations, experiments, and
445 mechanisms, *Rev. Geophys.*, 50, RG2004. <https://doi.org/10.1029/2011RG000382>

446 Masterlark, T., DeMets, T. C., and Wang, H. F. (2001). Homogeneous vs heterogeneous subduction zone models:
447 Coseismic and postseismic deformation. *Geophysical Research Letters* 28(21): 4047-4050.
448 <https://doi.org/10.1029/2001GL013612>

449 Masterlark, T., and Wang, H. F. (2002). Transient Stress-Coupling Between the 1992 Landers and 1999 Hector
450 Mine, California, Earthquakes. *Bulletin of the Seismological Society of America*. 92 (4), 1470–1486.
451 <https://doi.org/10.1785/0120000905>

452 Masterlark, T., (2003). Finite element model predictions of static deformation from dislocation sources in a
453 subduction zone: sensitivities to homogeneous, isotropic, Poisson-solid, and half-space assumptions.
454 *J. Geophys. Res., Solid Earth* 108 (B11). <https://doi.org/10.1029/2002JB002296>.

455 McCormack, K. A., and Hesse, M. A. (2018). Modeling the poroelastic response to megathrust earthquakes: A look
456 at the 2012 Mw 7.6 Costa Rican event. *Advances in Water Resources*, 114, 236–248.
457 <https://doi.org/10.1016/j.advwatres.2018.02.014>

458 McCormack, K., Hesse, M. A., Dixon, T. H., and Malservisi, R. (2020). Modeling the contribution of poroelastic
459 deformation to postseismic geodetic signals. *Geophysical Research Letters*, 47, e2020GL086945.
460 <https://doi.org/10.1029/2020GL086945>

461 Melgar, D., Riquelme, S., Xu, X., Baez, J.C., Geng, J., Moreno, M. (2017). The first since 1960: a large event in the
462 Valdivia segment of the Chilean Subduction Zone, the 2016 M7.6 Melinka earthquake. *Earth Planet. Sci.*
463 *Lett.* 474, 68–75. <https://doi.org/10.1016/j.epsl.2017.06.026>

464 Miller, S., Collettini, C., Chiaraluce, L. et al. (2004). Aftershocks driven by a high-pressure CO₂ source at depth.
465 Nature 427, 724–727. <https://doi.org/10.1038/nature02251>

466 Moreno, M., Melnick, D., Rosenau, M., Baez, J., Klotz, J., Oncken, O., al. (2012). Toward understanding tectonic
467 control on the Mw 8.8 2010 Maule Chile earthquake, Earth and Planetary Science Letters, 321–322,
468 152–165. <https://doi.org/10.1016/j.epsl.2012.01.006>

469 Oncken, O., Angiboust, S., Dresen, G. (2021). Slow slip in subduction zones: Reconciling deformation fabrics with
470 instrumental observations and laboratory results. Geosphere. <https://doi.org/10.1130/GES02382.1>

471 Peña, C., Heidbach, O., Moreno, M., Melnick, D., and Oncken, O. (2021). Transient Deformation and stress Patterns
472 Induced by the 2010 Maule Earthquake in the Illapel Segment. Front. Earth Sci. 9, 644834.
473 <https://doi.org/10.3389/feart.2021.644834>

474 Peña, C., Heidbach, O., Moreno, M., Bedford, J., Ziegler, M., Tassara, A., & Oncken, O. (2020). Impact of power-
475 law rheology on the viscoelastic relaxation pattern and afterslip distribution following the 2010 Mw 8.8
476 Maule earthquake. Earth and Planetary Science Letters 542, 116292.
477 <https://doi.org/10.1016/j.epsl.2020.116292>

478 Peña, C., Heidbach, O., Moreno, M., Bedford, J., Ziegler, M., Tassara, A., & Oncken, O. (2019). Role of Lower
479 Crust in the Postseismic Deformation of the 2010 Maule Earthquake: Insights from a Model with Power-
480 Law Rheology. Pure and Applied Geophysics. <https://doi.org/10.1007/s00024-018-02090-3>

481 Perfettini, H., Frank, W. B., Marsan, D., & Bouchon, M. (2018). A model of aftershock migration driven by
482 afterslip. Geophysical Research Letters, 45, 2283– 2293. <https://doi.org/10.1002/2017GL076287>

483 Press, W., A. Teukolsky, W. Vetterling, and B. Flannery (2002), Numerical Recipes in C: the Art of Scientific
484 Computing, Cambridge Univ Press, Cambridge, U. K.

485 Ranalli, G., (1997). Rheology and deep tectonics. Ann. Geofis..XL (3), 671–780. <https://doi.org/10.4401/ag-3893>.

486 Rolandone, F., Nocquet, J.-M., Mothes, P. A., Jarrin, P., Vallée, M., Cubas, N., et al. (2018). Areas prone to slow
487 slip events impede earthquake rupture propagation and promote afterslip. Sci. Adv. 4 (1), eaa06596.
488 <http://doi.org/10.1126/sciadv.aao6596>

489 Soto, H., Sippl, C., Schurr, B., Kummerow, J., Asch, G., Tilmann, F., et al. (2019). Probing the northern Chile
490 megathrust with seismicity: the 2014 M8.1 iquique earthquake sequence. Journal of Geophysical Research:
491 Solid Earth, 124, 12935–12954. <https://doi.org/10.1029/2019JB017794>

492 Sudhaus, H. and Jónsson, S. (2009). Improved source modelling through combined use of InSAR and GPS under
493 consideration of correlated data errors: application to the June 2000 Kleifarvatn earthquake, Iceland.
494 Geophysical Journal International, 176, 389-404. <https://doi.org/10.1111/j.1365-246X.2008.03989.x>

495 Sun, T., & Wang, K. (2015). Viscoelastic relaxation following subduction earthquakes and its effects on afterslip

496 determination. *Journal of Geophysical Research Solid Earth*, 120, 1329–1344.
497 <https://doi.org/10.1002/2014JB011707>.

498 Sun, T., Wang, K., Iinuma, T., Hino, R., He, J., Fujimoto, H., Kido, M., Osada, Y., Miura, S., Ohta, Y., Hu, Y.
499 (2014). Prevalence of viscoelastic relaxation after the 2011 Tohoku-oki earthquake. *Nature*, 514 (7520),
500 84–87. <https://doi.org/10.1038/nature13778>.

501 Tassara, A., Götze, H. J., Schmidt, S., and Hackney, R. (2006). Three-dimensional density model of the Nazca plate
502 and the Andean continental margin. *J. Geophys. Res. Solid Earth*, 111(B9).
503 <https://doi.org/10.1029/2005JB003976>

504 Toda, S., Lin, J. & Stein, R.S. (2011). Using the 2011 Mw 9.0 off the Pacific coast of Tohoku Earthquake to test the
505 Coulomb stress triggering hypothesis and to calculate faults brought closer to failure. *Earth Planet Sp.*, 63,
506 39. <https://doi.org/10.5047/eps.2011.05.010>

507 Tsang, L. L. H., Vergnolle, M., Twardzik, C., Sladen, A., Nocquet, J.-M., Rolandone, F., et al. (2019). Imaging
508 rapid early afterslip of the 2016 Pedernales earthquake, Ecuador. *Earth Planet. Sci. Lett.* 524, 115724.
509 <https://doi.org/10.1016/j.epsl.2019.115724>

510 Tung, S., and Masterlark, T. (2018). Delayed poroelastic triggering of the 2016 October Visso earthquake by the
511 August Amatrice earthquake, Italy. *Geophysical Research Letters* 45(5), 2221-2229.
512 <https://doi.org/10.1002/2017GL076453>

513 Wallace, L. M., Webb, S. C., Ito, Y., Mochizuki, K., Hino, R., Henrys, S., et al. (2016). Slow slip near the trench at
514 the Hikurangi subduction zone, New Zealand. *Science*, 352(6286), 701–704.
515 <https://doi.org/10.1126/science.aaf2349>

516 Wang, H.F., 2000. *Theory of Linear Poroelasticity: With Applications to Geomechanics*. Princeton University Press,
517 Princeton.

518 Wang, K., Hu, Y., & He, J. (2012). Deformation cycles of subduction earthquakes in a viscoelastic Earth, *Nature*,
519 484(7394), 327–332. <https://doi.org/10.1038/nature11032>

520 Warren-Smith, E., Fry, B., Wallace, L. et al. (2019). Episodic stress and fluid pressure cycling in subducting oceanic
521 crust during slow slip. *Nat. Geosci.* 12, 475–481. <https://doi.org/10.1038/s41561-019-0367-x>

522 Weiss, J. R., Walters, R. J., Morishita, Y., Wright, T. J., Lazecky, M., & Wang, H., et al. (2020). High-resolution
523 surface velocities and strain for Anatolia from Sentinel-1 InSAR and GNSS data. *Geophysical Research*
524 *Letters*, 47, e2020GL087376. <https://doi.org/10.1029/2020GL087376>

525 Weiss, J. R., Qiu, Q., Barbot, S., Wright, T. J., Foster, J. H., Saunders, A., et al. (2019). Illuminating subduction
526 zone rheological properties in the wake of a giant earthquake. *Science advances*, 5(12), eaax6720.
527 <http://doi.org/10.1126/sciadv.aax6720>

- 528 Wegmüller, U., & Werner, C. (1997). Gamma SAR processor and interferometry software, Proc. of the 3rd ERS
529 Scientific Symposium on space at the service of our environment, 14-21 March 1997, Florence Italy.
- 530 Welstead, S. T. (1999), Fractal and Wavelet Image Compression Techniques, 232 pp., SPIE Opt. Eng., Bellingham,
531 Washington.
- 532 Werner, C., Wegmüller, U., Frey, O., Santoro, M. (2011). Interferometric processing of PALSAR wide-beam
533 ScanSAR data, Fringe 2011, 8th International Workshop on "Advances in the Science and Applications of
534 SAR Interferometry", 19-23 Sep 2011, Frascati, Italy.
- 535 Williamson, A.L., and Newman, A.V., (2018). Limitations of the resolvability of finite-fault models using static
536 land-based geodesy and open-ocean tsunami waveforms. *Journal of Geophys. Res., Solid Earth*, 123(10),
537 9033-9048. <https://doi.org/10.1029/2018JB016091>
- 538 Wright, T. J., Parsons, B. E., and Lu, Z. (2004). Toward mapping surface deformation in three dimensions using
539 InSAR, *Geophys. Res. Lett.*, 31, L01607. <https://doi.org/10.1029/2003GL018827>
- 540 Yang, H., Guo, R., Zhou, J., Yang, H., Sun, H. (2022). Transient poroelastic response to megathrust earthquakes: a
541 look at the 2015 Mw 8.3 Illapel, Chile, event. *Geophysical Journal International*, ggac099,
542 <https://doi.org/10.1093/gji/ggac099>